



# High DHA selectivity and low-cost electrode for glycerol oxidation: CuO regulates MnO<sub>2</sub> electron density to promote DHA desorption

Zijian Huang, Hongji Ren, Jian Guo, Ya Tang, Daixin Ye<sup>\*</sup>, JiuJun Zhang, Hongbin Zhao<sup>\*</sup>

Department of Chemistry, College of Sciences, Shanghai University, No. 99, Shangda Road, Shanghai 200444, China

## ARTICLE INFO

### Keywords:

Glycerol oxidation reaction  
Electrocatalyst  
DHA  
Electron density  
MnO<sub>2</sub>

## ABSTRACT

Glycerol oxidation reaction (GOR) is an attractive alternative reaction for oxygen evolution reaction (OER) in the electrochemical water splitting and can be used to generate high-value products. However, the development of GOR electrocatalysts with high catalytic activity and low cost is challenging. In this research, a self-supported copper-manganese electrode (MnO<sub>2</sub>-CuO/CF) was developed, which attains a current density of 10.7 mA cm<sup>-2</sup> at a low potential of 1.3 V, while yielding 1,3-dihydroxyacetone (DHA), with a selectivity of 60%. DFT calculations reveal the synergistic effect between CuO and MnO<sub>2</sub>, enhancing glycerol adsorption. Additionally, the overlap configuration of CuO and MnO<sub>2</sub> results in a lower electron density on MnO<sub>2</sub>, preventing further oxidation and increasing DHA selectivity. By coupling GOR and water electrolysis, the dual output of high value-added organic products and high-purity hydrogen can be realized, which provides a new idea for green hydrogen production and electrochemical synthesis of high value-added chemicals.

## 1. Introduction

As fossil fuel reserves continue to diminish, the quest for clean and sustainable energy alternatives has become paramount in addressing the contemporary energy crisis[1,2]. Hydrogen, as a pristine and environmentally benign energy source, has captured the focus of researchers[3]. In particular, water electrolysis has emerged as a prominent method for producing green hydrogen energy. This approach is favored for its cost-effective raw materials, environmental friendliness, and absence of carbon emissions.

The electrochemical water splitting involves two half-reactions: the cathodic hydrogen evolution reaction (HER) and the anodic OER[4,5]. Unlike HER, oxygen evolution reaction (OER) is a multifaceted process that encompasses four electron transfer steps. The presence of OER requires a higher voltage for the effective electrolysis of water[6]. Moreover, oxygen, as the main product of OER, holds limited economic value. Conversely, opting for the thermodynamically more favorable oxidation of small molecules (such as hydrazine, alcohols, urea), rather than OER, not only significantly reduces the anodic overpotential but also allows for the oxidation of organic small molecules to generate high-value products, thus enhancing economic returns[7–11]. Additionally, this approach effectively mitigates safety concerns stemming from the mixture of hydrogen and oxygen[12–14].

Glycerol is a waste product derived from the synthesis of biodiesel, and the rapid growth of the biodiesel industry has led to an overproduction of glycerol[15–17]. Glycerol is inexpensive and renewable, and the products it converts have high economic value. Moreover, Glycerol oxidation reaction (GOR) has low thermodynamic potential, therefore, it can be a good candidate to replace OER. Compared to other small molecule oxidation reactions (hydrazine, urea) that replace OER, the products of GOR have higher economic value and the C3 products are usually more expensive than C1 products[18]. Among the oxidation products of glycerol, 1,3-dihydroxyacetone (DHA) emerges as a versatile additive with significant economic value. It finds applications in the cosmetic, pharmaceutical, and food industries[19]. The electro-oxidation of glycerol, coupled with hydrogenolysis, offers a dual benefit: the production of green hydrogen energy alongside valuable products[20].

Currently, significant strides have been achieved in the investigation of glycerol electrooxidation, predominantly focusing on catalytic oxidation using noble metals, with particular emphasis on the mechanism catalyzed by platinum-based materials[21–24]. Nonetheless, their exorbitant cost poses a substantial hurdle for the commercial viability of glycerol electrooxidation. In recent years, exploration on earth-abundant transition metal catalysts, particularly those based on copper and nickel, has played a pivotal role in advancing non-precious

<sup>\*</sup> Correspondence to: Department of Chemistry & Institute for Sustainable Energy, College of Sciences, Shanghai University, Shanghai 200444, PR China.

E-mail addresses: [daixinye@shu.edu.cn](mailto:daixinye@shu.edu.cn) (D. Ye), [hongbinzhao@shu.edu.cn](mailto:hongbinzhao@shu.edu.cn) (H. Zhao).

metal glycerol electrooxidation[13]. Previously, researchers achieved remarkable selectivity for DHA at low current densities ( $3 \text{ mA cm}^{-2}$ ) using copper oxide as the catalytic material[25]. Therefore, searching for catalysts to enhance the catalytic efficacy for glycerol is imperative. In the context of GOR, manganese-based catalysts are also promising candidates.  $\text{MnO}_2$  can catalyze the conversion of glycerol into formic acid under acidic conditions, with a protective mechanism that ensures the stability of  $\text{MnO}_2$  in such environments[26]. In alkaline conditions, various manganese dioxide species demonstrate the ability to catalyze glycerol oxidation, yielding DHA[27]. However, they generally require catalytic oxidation at higher voltages, and the selectivity of DHA is less than 50%. Composite materials are composed of two or more different materials, and their combination may produce synergistic effects, making their performance superior to individual components[28]. In previous reports, CuO can increase the redox ability of manganese ions while weakening the Mn-O bond[29,30]. Designing manganese copper based composite catalyst can be an important approach to obtain DHA by GOR.

In this study, we developed a copper-manganese self-supported electrode,  $\text{MnO}_2\text{-CuO/copper foam (CF)}$ , which shows high catalytic activity and selectivity to produce DHA.  $\text{MnO}_2\text{-CuO/CF}$  was able to oxidize glycerol at 1.3 V vs. RHE, yielding DHA with a selectivity of up to 60%. The overlap configuration resulting from the combination of lamellae and dendrites of  $\text{MnO}_2\text{-CuO/CF}$  accelerates the electron transfer and the diffusion of reactants and products. The DFT results implied a synergistic effect in the  $\text{MnO}_2\text{-CuO/CF}$  electrode: the similar adsorption of secondary hydroxyl groups enhanced glycerol adsorption, while the lower electron density of  $\text{MnO}_2$  facilitated DHA desorption. Furthermore, a plausible mechanism for the catalytic oxidation of glycerol was proposed, according to density functional theory (DFT), high-performance liquid chromatography (HPLC), and Raman spectroscopy analyses. In this study, we successfully developed a high-efficiency, low-energy consumption GOR electrocatalyst to obtain DHA, and provided a new idea for hydrogen production by electrolysis of water.

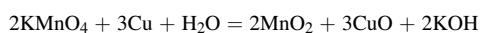
## 2. Experimental section

### 2.1. Materials and chemicals

Potassium permanganate ( $\text{KMnO}_4$ ), sulfuric acid ( $\text{H}_2\text{SO}_4$ ), manganese sulfate ( $\text{MnSO}_4$ ), acetone, hydrochloric acid, potassium hydroxide, glyceric acid, glycerol, glyceraldehyde, glycolic acid, oxalic acid, formic acid, acetic acid, tartaric acid and copper foam (2 mm) were purchased from Macklin. All reagents were analytical reagent (AR).

### 2.2. Synthesis of $\text{MnO}_2\text{-CuO/CF}$ , $\text{CuO/CF}$ , and $\text{MnO}_2\text{/CF}$

$\text{MnO}_2\text{-CuO/CF}$  was synthesized through a straightforward one-step hydrothermal method. Initially, a copper foam ( $3 \text{ cm} \times 5 \text{ cm}$ ) was cleansed with hydrochloric acid, acetone, deionized (DI) water, and ethanol for 15 minutes, followed by drying in a vacuum oven. Typically, a solution consisting of  $\text{KMnO}_4$  (0.01 mol) and  $\text{H}_2\text{SO}_4$  (5  $\mu\text{L}$ ) was dissolved in 40 mL of DI water. After stirring for 1 hour, the reaction solution and the copper foam were placed inside a 50 mL Teflon-lined stainless-steel autoclave, sealed, and subjected to a 12-hour reaction at  $150^\circ\text{C}$ . Subsequent to the reaction, the copper foam was washed with DI water for 3 times, and then dried in a vacuum oven at  $60^\circ\text{C}$  for 24 hours. In neutral and mildly acidic conditions, the reaction between potassium permanganate and copper proceeds as follows:



$\text{CuO/CF}$  was synthesized following a comparable procedure. The treated copper foam was positioned within a 25 mL Teflon liner, to which 20 mL of DI water and 1 mL of a 20%  $\text{H}_2\text{O}_2$  solution were added.

Subsequently, the reactor liner was sealed using a stainless-steel casing, and the reaction was conducted at  $150^\circ\text{C}$  for 8 hours. After the reaction, the  $\text{CuO/CF}$  was washed with DI water for 3 times, and then dried in a vacuum oven at  $60^\circ\text{C}$  for 24 hours.

$\text{MnO}_2\text{/CF}$  was synthesized using a previously reported method[31]. 0.54 mg of  $\text{MnSO}_4$  was dissolved in 500 mL of DI water and stirred vigorously for 40 minutes. Subsequently, 50 mL of DI water containing 0.38 g of  $\text{KMnO}_4$  was added peristaltically at a flow rate of 1 mL/min. The resulting  $\text{MnO}_2$  was collected through centrifugation and then subjected to lyophilization at  $-40^\circ\text{C}$  overnight. The obtained  $\text{MnO}_2$  mixed with nafion solution to get an ink, which was subsequently coated on the cleaned copper foam to obtain  $\text{MnO}_2\text{/CF}$ .

### 2.3. Materials characterization

The microscopic morphology of the catalyst was characterized by using scanning electron microscopy (SEM, benzene phase Pharos G2, 15 kV). The Pharos G2 was equipped with an energy-dispersive spectroscopy (EDS) system, which was used to characterize composition of the catalyst.

The sample for transmission electron microscope (TEM, JEM2100F, 200 eV) was prepared by dispersing the surface of  $\text{MnO}_2\text{-CuO/CF}$  in anhydrous ethanol and then moving it onto a porous carbon support membrane on a copper grid.

The X-ray diffraction (XRD) patterns were conducted by DX-2700 (Cu-K $\alpha$  radiation ( $\lambda=1.54056 \text{ \AA}$ ) with the  $2\theta$  range from  $10^\circ$  to  $90^\circ$  and a scan rate of  $5^\circ \text{ min}^{-1}$ .

X-ray photoelectron spectroscopy (XPS, Thermo Scientific K-ALPHA) was used to analyze the surface chemistry valence of  $\text{MnO}_2\text{-CuO/CF}$ ,  $\text{CuO/CF}$  and  $\text{MnO}_2$ . The excitation source using operating voltage 12.5 kV, Al K $\alpha$  rays, current 16 mA and 10 cycles of signal accumulation. The pass energy was set to 50 eV, and the energy step size was 0.1 eV. The vacuum chamber pressure is  $8 \times 10^{-10} \text{ Pa}$ . The Binding Energy (BE) value was corrected for the charging effect, setting the value of the C1s line with indefinite carbon at 284.8 eV. Meanwhile, the surface chemistry valence of  $\text{MnO}_2\text{-CuO/CF}$  before and after the GOR reaction were also measured by XPS.

### 2.4. Electrochemical measurements

This GOR was investigated in a traditional three-electrode cell system employing a PARSTAT 3000 A electrochemical workstation. For these electrochemical measurements, an H-type electrolytic cell, which effectively separates the counter electrode from the working electrode to prevent the reduction of glycerol oxidation products, was used. RE, WE, and CE correspond to the reference electrode (Hg/HgO in an alkaline solution), the working electrode ( $\text{MnO}_2\text{-CuO/CF}$ ,  $1 \text{ cm}^2$ ), and the counter electrode (platinum sheet,  $1 \text{ cm}^2$ ), respectively. All GOR tests conducted in alkaline conditions were carried out in a 1 M KOH solution. The electrochemical characteristics of  $\text{CuO/CF}$  and  $\text{MnO}_2\text{/CF}$  were evaluated as part of the comparison group under identical experimental conditions.

The liquid-phase products resulting from glycerol electrooxidation were analyzed using high-performance liquid chromatography (HPLC). In alkaline conditions, all electrooxidation products of glycerol were expected to be in the form of salts. For the sake of simplicity, the term 'acid' is used in the subsequent narrative. The specific testing procedure was as follows: 1 mL of the solution after chronoamperometry testing was taken, and concentrated sulfuric acid was added to adjust the solution to slightly acidic ( $\text{pH} = 6$ ). The solution was filtered through a  $0.22 \mu\text{m}$  filter and injected into the column for analysis. The detection column consisted of a guard column (Bio-Rad,  $4.6 \times 30 \text{ mm}$ ) and a primary column (Shodex Sugar SH1011,  $8 \times 300 \text{ mm}$ ). The mobile phase used was 0.5 M  $\text{H}_2\text{SO}_4$ , and the column temperature was maintained at  $65^\circ\text{C}$ . The detection flow rate was set at  $0.4 \text{ mL min}^{-1}$ , and the analysis of a single sample required 30 minutes. The glycerol oxidation

products, separated by the column, were detected using a tandem refractive index detector (RID, SHIMADZU, RID-10A) and a diode array detector (DAD). An external standard method was employed to create a standard curve for all potential oxidation products, including glycerol, glyceric acid (GLA), glyceraldehyde (GLAD), oxalic acid (OA), glycolic acid (GA), acetic acid (HAC), DHA, formic acid (FA), and tartaric acid (TA).

## 2.5. DFT calculations

To investigate the adsorption pattern of molecules on MnO<sub>2</sub>-CuO/CF and gain insight into the reaction mechanism of glycerol oxidation to DHA, we conducted spin-polarized density functional theory (DFT) calculations. All DFT computations employed the Vienna Ab initio Simulation Package (VASP) within the spin-polarization framework, utilizing the Perdew-Burke Ernzerhof (PBE) functional[32–37]. We introduced the Hubbard U correction to improve calculation accuracy, the effective U-J (Ueff) parameter was determined to be 7.0 eV for the metallic copper atom and 4.0 eV for the metallic manganese atom to recover the effect of 3d electron correlation[38–40]. In the iterative solution of the Kohn-Sham equation, the energy criterion was set to 10<sup>−5</sup> eV. We employed a Projection-Augmented Wave (PAW) potential to represent ion nuclei, and the valence electrons were computed using plane waves. Valence electron calculations utilized plane waves with a kinetic energy cutoff of 450 eV. Geometry optimization was pursued until the Hermann-Feynman force on each atom was less than 0.03 eV. Å<sup>−1</sup>.

In the case of MnO<sub>2</sub> (100), we utilized a 3 × 2 × 1 Monkhorst-Pack k-points grid, while for CuO (111), a 3 × 3 × 1 Monkhorst-Pack k-points grid was applied. Throughout all calculations, atomic positions were allowed to relax. The MnO<sub>2</sub> (100) model exhibited lattice parameters of a = 5.8433 Å, b = 10.5856 Å and c = 22.5915 Å, encompassing a thickness of 10 at. layers with 15 Å vacuum above. For CuO (111), the lattice parameters were a = 11.6269 Å and b = 11.9776 Å, c = 20.8209 Å with a thickness of 9 at. layers and 15 Å of vacuum space above. The adsorption energy is regarded as a measure of the strength of adsorbate-substrate adsorption. The adsorption energies of all adsorbed molecules are calculated according to the following formula:

$$E_{\text{ads}} = E_{\text{adsorbate/slab}} - E_{\text{adsorbate}} - E_{\text{slab}}$$

Where  $E_{\text{adsorbate/slab}}$ ,  $E_{\text{adsorbate}}$ , and  $E_{\text{slab}}$  denote the total energy of the CuO (111) or MnO<sub>2</sub> (100) surface and the adsorbed molecule, the energy of free adsorbed molecule in the vacuum, and the energy of the CuO (111) or MnO<sub>2</sub> (100) surface, respectively. With this definition, a negative adsorption energy corresponds to a stable adsorption[41].

## 3. Results and discussion

### 3.1. Catalyst characterizations

The synthesis of MnO<sub>2</sub>-CuO/CF is elucidated in Fig. 1. A method employing in-situ hydrothermal growth was employed to obtain a stable and uniformly distributed catalytic electrode. In this approach, copper

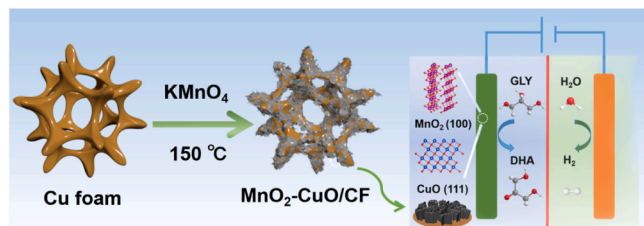


Fig. 1. Schematic of the synthesis of MnO<sub>2</sub>-CuO/CF and the application in GOR and HER.

foam (Fig. S1) served both as catalyst carrier and copper source during synthesis. The MnO<sub>2</sub>-CuO/CF crystal structure was analyzed through XRD. Given that only the surface layer of the copper foam was enriched with CuO and MnO<sub>2</sub>, signal interference from copper was inevitable in the detection process. The XRD pattern in Fig. 2a displays prominent copper peaks (marked with star). Additionally, MnO<sub>2</sub>-CuO/CF exhibits clear diffraction peaks at 2θ values of 35.6, 38.8, and 48.9, corresponding to cubic CuO (JCPDS 78–0428) (111), (200), and (220), respectively. Owing to the limited MnO<sub>2</sub> content within the material and low crystalline quality, the diffraction peaks associated with MnO<sub>2</sub> were not directly discernible. To mitigate the influence of copper oxide and copper foam on the test outcomes, a diluted sulfuric acid was employed to dissolve and eliminate the copper oxide. The filter residue was subsequently subjected to XRD analysis. As displayed in Fig. 2b, the three most prominent diffraction peaks at 2θ of 37.1, 56.0, and 66.7, correspond to ε-MnO<sub>2</sub> (JCPDS 30–0820) (100), (102), and (110), respectively.

MnO<sub>2</sub>-CuO/CF was successfully synthesized in situ on the copper foam surface through a hydrothermal reaction. Under high temperature and pressure, the copper foam, serving as the source of copper, undergoes a redox reaction with potassium permanganate under neutral conditions. This results in the stable growth of a overlap configuration of CuO and MnO<sub>2</sub> on the copper foam surface. SEM image (Fig. 2c) shows a uniform network structure composed of 20 nm-thick sheets and 40 nm-diameter rods. Subsequently, TEM image (Fig. 2d) shown lattice fringes of the electrode surface layer, which demonstrated that the primary exposed crystal plane is the ε-MnO<sub>2</sub> (100) crystal plane. SEM and TEM images reveal that the surface of MnO<sub>2</sub>-CuO/CF primarily comprises ε-MnO<sub>2</sub>.

To gain further insight into the distribution of CuO and MnO<sub>2</sub> on the copper foam surface, we conducted Energy Dispersive Spectrometer (EDS) analysis on a cross-sectional sample of MnO<sub>2</sub>-CuO/CF. The overlap configuration of CuO and MnO<sub>2</sub>, as depicted in Fig. 2e, CuO is predominantly concentrated near the smooth surface of the copper foam, while MnO<sub>2</sub> is primarily located in the outer region of the material. After a long period of ultrasonic cleaning to remove most of the manganese dioxide, copper oxide particles with a diameter of 50 nm to 100 nm growing on the surface of the copper foam was observed, as shown on Fig. S2. The SEM image of CuO/CF, prepared using similar method, closely resembles that of MnO<sub>2</sub>-CuO/CF post-ultrasonic cleaning, as illustrated in Fig. S3. Additionally, we conducted SEM characterization of ε-MnO<sub>2</sub>, as detailed in Fig. S4, which was also similar to the MnO<sub>2</sub>-CuO/CF.

The surface chemical properties of three different samples (MnO<sub>2</sub>-CuO/CF, CuO/CF& MnO<sub>2</sub>/CF) were studied by XPS (the wide scan survey spectra are shown in Fig. S5–7)[42,43]. As shown in Fig. 3a, b, it can be seen that BE (Cu2p<sub>3/2</sub>) = 933.1 eV; BE (Cu2p<sub>1/2</sub>) = 953.4 eV, which is consistent with CuO. To further verify this conclusion, the Auger peaks of MnO<sub>2</sub>-CuO/CF and CuO/CF were collected (Fig. 3c, d). Auger parameters were defined as Aug(Cu) = BE(Cu2p<sub>3/2</sub>) + KE (CuLMM), Aug(Cu) consistently match the literature values on copper oxide (MnO<sub>2</sub>-CuO/CF = 1851.4 eV; CuO/CF = 1851.7 eV)[44]. The Mn 2p<sub>3/2</sub> spectra (Fig. 3e, f) was deconvoluted into two peaks at 641.7 and 642.9 eV, corresponding to Mn<sup>3+</sup> and Mn<sup>4+</sup>, respectively[27]. It can be seen that the content of Mn<sup>4+</sup> in MnO<sub>2</sub>-CuO/CF is significantly higher than that in MnO<sub>2</sub>/CF. By collecting Mn3s spectra, this peak separation (ΔE) can be calculated, thereby calculating the average oxidation state (AOS; AOS = 8.956 – 1.126 \* ΔE)[45]. The AOS of these two samples are 3.51 (MnO<sub>2</sub>-CuO/CF) and 3.30 (MnO<sub>2</sub>/CF), which is consistent with Fig. 3c,f.

### 3.2. Glycerol electrooxidation reaction and product analysis

The theoretical oxidation potential of glycerol (0.003 V vs· RHE) was significantly lower than that of OER (1.23 V vs· RHE)[46]. Replacing OER with GOR can reduce energy consumption while generating high



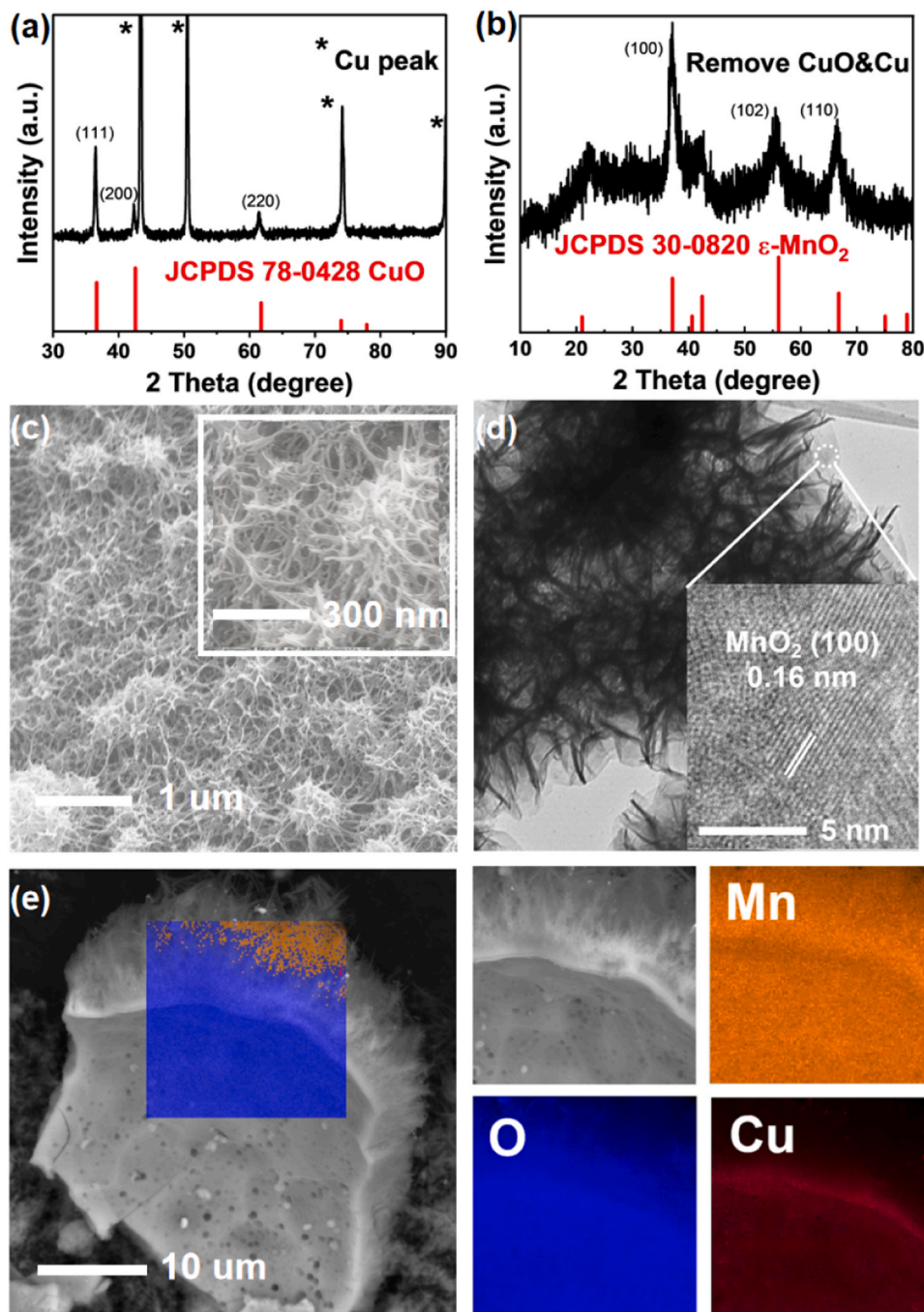


Fig. 2. The characterizations of  $\text{MnO}_2\text{-CuO/CF}$ : (a, b) XRD patterns, (c) SEM image, (d) TEM image, (e) EDS element mapping images.

value-added products. The catalytic activity evaluations for these electrodes are presented in Fig. 4. Fig. 4a illustrates the linear scanning voltammetry (LSV) curves of the catalyst in a solution of 0.1 M glycerol dissolved in 1 M KOH, as well as in the absence of glycerol. Notably, the GOR attains a current density of  $10.7 \text{ mA cm}^{-2}$  at 1.30 V vs. RHE, whereas the onset potential for the OER is 1.6 V vs. RHE. The Tafel slope, an important parameter for catalyst evaluation, is presented in Fig. 4b for both GOR and OER. Specifically, the Tafel slope for GOR is  $113 \text{ mV dec}^{-1}$ , which is significantly lower than that of OER ( $188 \text{ mV dec}^{-1}$ ). These differences confirm that GOR exhibits more favorable electrocatalytic kinetics compared to OER.

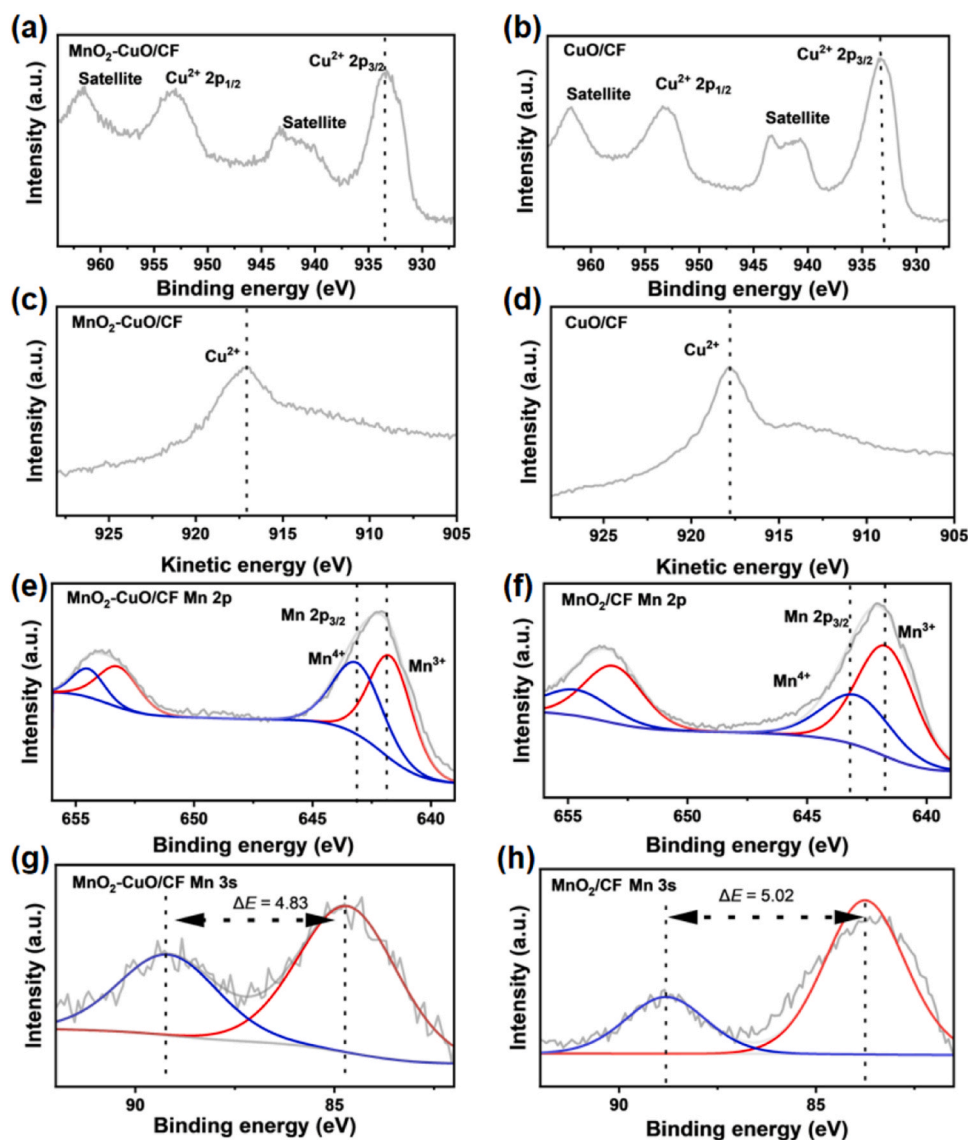
Voltage represents a pivotal parameter influencing GOR. We conducted experiments to examine the chronoamperometry curves of glycerol electrooxidation at four different voltages (as depicted in

Fig. 4c). The decrease in current observed at elevated voltages primarily arises from the depletion of glycerol within the reaction. The Faraday efficiency of glycerol electrooxidation was determined using the following equation.

$$FE(\%) = \frac{N}{Q/(Z \times F)} \times 100\%$$

where  $FE$  stands for Faraday efficiency, and  $N$  and  $Z$  represent the productivity of product and the corresponding number of electron transfers, respectively;  $F$  is the Faraday constant ( $96485 \text{ C mol}^{-1}$ ), and  $Q$  is the total charge. In Fig. 4d, it is evident that glycerol achieves a Faraday efficiency exceeding 90% at both 1.2 V and 1.3 V. The decline in Faraday efficiency under higher voltage conditions can be attributed to the complete oxidation of glycerol to carbonate. This study did not





**Fig. 3.** The XPS spectra of MnO<sub>2</sub>-CuO/CF: (a) Cu 2p, (c) Auger Cu LMM, (e) Mn 2p, (g) Mn 3s; CuO/CF: (b) Cu 2p, (d) Auger Cu LMM; MnO<sub>2</sub>/CF: (f) Mn 2p, (h) Mn 3s.

consider carbonate or carbon dioxide as valuable GOR products, and consequently, their production was not detected in subsequent analyses. The selectivity of a specific product can be expressed by following equation. Where  $N$  represents the yield of the product.

$$\text{Selectivity}(\%) = \frac{N(\text{specific product})}{N(\text{all products})} \times 100\%$$

The analysis of oxidation products was carried out using high-performance liquid chromatography (HPLC). For the quantification of GOR products, we established calibration curves using different standard sample concentrations, allowing us to measure the various GOR products based on the chromatographic data collected (as shown in Fig. S8-S10). The selectivity of GOR products was subject to further analysis through HPLC, as depicted in Fig. 4e. The main products derived from GOR at 1.3 V were identified as DHA and formic acid. The content of these two main products displayed a noticeable upward trend, as depicted in Fig. 4f, highlighting the stable proportion of these electrochemical products over time. The average selectivity of DHA reached 60%, while the total selectivity of the two main products, formic acid and DHA, consistently exceeded 95%. The analysis of GOR products at other voltages are shown in Fig. S11-S13. At potentials lower than 1.3 V,

glycerol exhibits diminished conversion rates, while under voltage higher than 1.4 V, glycerol undergoes intense oxidation, leading to fast formation of formic acid. In summary, voltage is a critical factor influencing glycerol oxidation products, and precise voltage control indicates that at 1.3 V, the current density can reach  $10.7 \text{ mA cm}^{-2}$  while achieving a high DHA selectivity of up to 60%. As the voltage increases from 1.2 V to 1.4 V, the current density increases from  $2.0 \text{ mA cm}^{-2}$  to  $32.5 \text{ mA cm}^{-2}$ . The concentration of DHA decreases from 60% to 35%, the concentration formic acid increases from 31% to 55%, confirming that oxidation potential is related to that of selectivity. Table 1 shows the comparison of different GOR catalysts performance. Typically, precious metal catalysts have high DHA selectivity and typically react at low voltage with low current density. The high cost of precious metals limits their large-scale application. Non precious metal catalysts are generally carried out under alkaline conditions, but strong alkalinity is beneficial for the cleavage of C-C bonds, resulting in a decrease in DHA selectivity [51]. Therefore many studies have used Na<sub>2</sub>B<sub>4</sub>O<sub>7</sub> as an electrolyte. The MnO<sub>2</sub>-CuO/CF has high selectivity of DHA while reducing the reaction voltage, which can effectively reduce energy consumption of GOR.

To explore the mechanism of GOR, we compared electrochemical performance of CuO/CF and MnO<sub>2</sub>/CF. As depicted in Fig. 5a, the

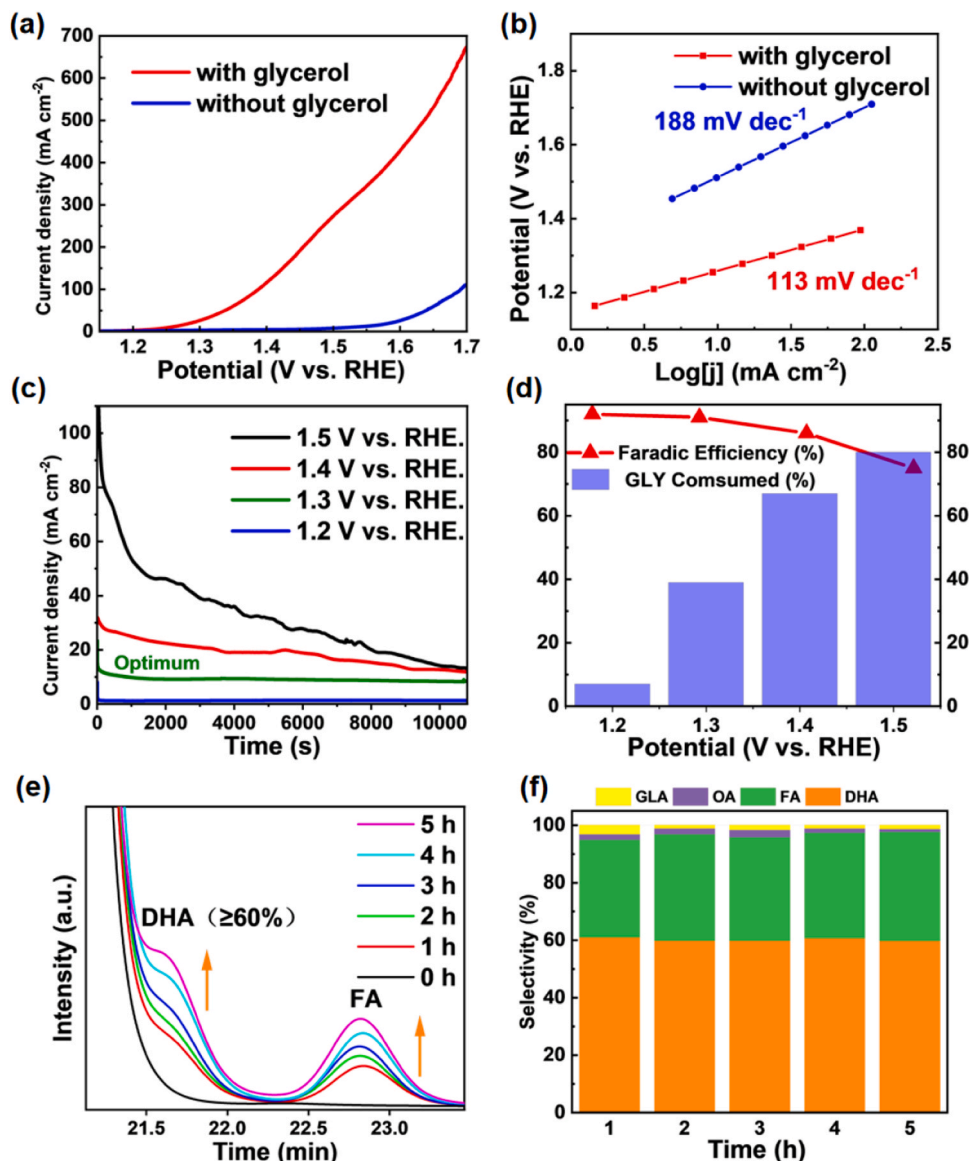


**Fig. 4.** (a) Comparison of GOR and OER polarization curves for MnO<sub>2</sub>-CuO/CF. (b) Corresponding Tafel slope for GOR and OER. (c) Chronoamperometry at potential of 1.2, 1.3, 1.4, and 1.5 V. (d) GLY consumed(%) obtained from HPLC with different applied potential. (e) HPLC chromatogram of main product at 1.3 V. (f) Products selectivity obtained from HPLC at 1.3 V.

**Table 1**  
GOR products by other catalysts.

Catalyst	Electrolyte	Potential and current density	Product selectivity (%)
PtSb/C [47]	0.1 M glycerol & 0.5 M H <sub>2</sub> SO <sub>4</sub>	0.797 V vs.SHE 5.0 mA/cm <sup>2</sup>	DHA 60%
Pt <sub>5</sub> Ru <sub>5</sub> /C [48]	0.5 M glycerol & 0.5 M NaOH	1.1 V vs. SHE 3.5 mA/cm <sup>2</sup>	DHA 35%
CuO [25]	0.1 M glycerol & 0.1 M Na <sub>2</sub> B <sub>4</sub> O <sub>7</sub>	2.06 V vs. RHE 3.0 mA/cm <sup>2</sup>	DHA 60%
γ-MnO <sub>2</sub> [27]	0.1 M glycerol & 0.1 M Na <sub>2</sub> B <sub>4</sub> O <sub>7</sub>	1.85 V vs. RHE 10.0 mA/cm <sup>2</sup>	DHA 50%
Co <sub>3</sub> O <sub>4</sub> [49]	0.1 M glycerol & 0.1 M Na <sub>2</sub> B <sub>4</sub> O <sub>7</sub>	1.7 V vs. RHE 1.0 mA/cm <sup>2</sup>	DHA 60%
MnO <sub>2</sub> [50]	0.1 M glycerol & 0.1 M Na <sub>2</sub> B <sub>4</sub> O <sub>7</sub>	2.05 V vs. RHE 6.0 mA/cm <sup>2</sup>	DHA 46%
MnO <sub>2</sub> -CuO/CF (This work)	0.1 M glycerol & 1 M KOH	1.3 V vs. RHE 10.7 mA/cm <sup>2</sup>	DHA 60%

current density of MnO<sub>2</sub>-CuO/CF is significantly higher than that of CuO/CF and MnO<sub>2</sub>/CF, confirming the superior catalytic activity of MnO<sub>2</sub>-CuO/CF. To avoid the impact of the OER, chronoamperometry tests were conducted on CuO/CF and MnO<sub>2</sub>/CF at 1.2 V, 1.3 V, and 1.4 V vs. RHE. The chronoamperometry test curves for CuO/CF and MnO<sub>2</sub>/CF are illustrated in Figs. 5b and 5c, the current density is only 4.0 mA cm<sup>-2</sup> and 2.1 mA cm<sup>-2</sup> at 1.3 V, respectively. It is evident that MnO<sub>2</sub>-CuO/CF exhibits a greater current density of 10.7 mA cm<sup>-2</sup> at 1.3 V, providing further evidence of its elevated catalytic activity. At 1.2 V, both CuO/CF and MnO<sub>2</sub>/CF exhibit lower catalytic activity, with a current density of only 0.3 mA cm<sup>-2</sup>. While when the voltage is up to 1.4 V, the current density of CuO/CF and MnO<sub>2</sub>/CF is only 10.5 mA cm<sup>-2</sup> and 4.8 mA cm<sup>-2</sup>. Subsequently, the product content in the electrolyte solution post-reaction was quantified using HPLC. The distribution statistics of these various products are detailed in Fig. 5d-f. The selectivity of the two primary products, DHA and formic acid, was relatively similar at 1.2 V vs. RHE. At 1.2 V, the current is below 3 mA/cm<sup>2</sup>, and both catalysts have low catalytic efficiency. The yield and selectivity of DHA are also low. As the voltage rose, the selectivity of

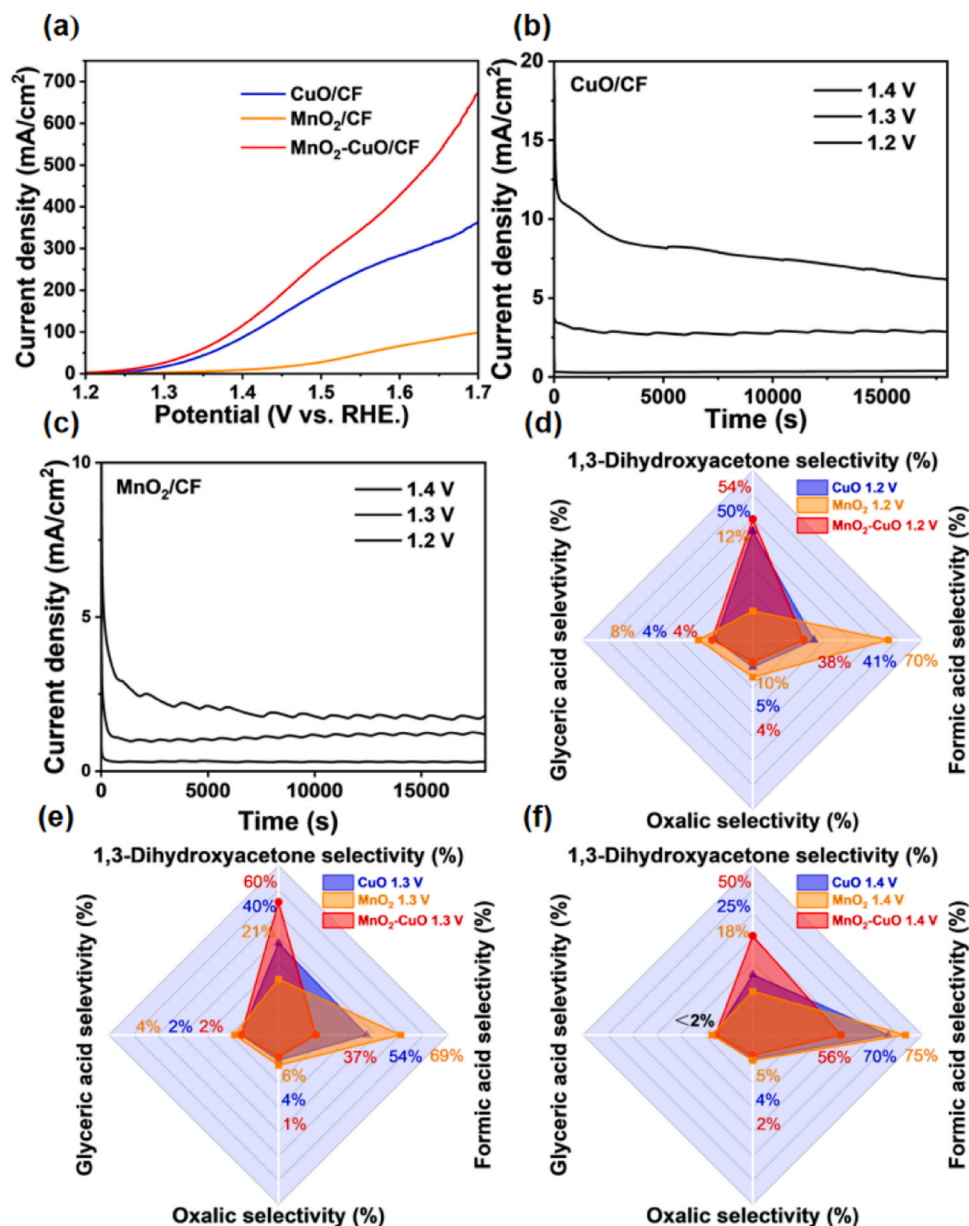


**Fig. 5.** (a) Comparison of MnO<sub>2</sub>-CuO/CF, MnO<sub>2</sub>/CF and CuO/CF polarization curves for GOR. (b, c) Chronoamperometry tests of CuO/CF and MnO<sub>2</sub>/CF at 1.2 V, 1.3 V, and 1.4 V vs. RHE. (d, e, f) Products selectivity obtained from HPLC at 1.2 V, 1.3 V, and 1.4 V vs. RHE.

formic acid catalyzed by CuO/CF notably increased, resulting in a substantial reduction in DHA content, with only 25% selectivity at 1.4 V. Meanwhile, MnO<sub>2</sub>/CF produces a large amount of inexpensive formic acid at all three voltages, while DHA has lower selectivity. Obviously, the development of MnO<sub>2</sub>-CuO/CF to oxidize glycerol is more commercially promising, as DHA has greater economic value, while the lower selectivity of other products reduces subsequent isolation and purification.

To evaluate the stability of MnO<sub>2</sub>-CuO/CF, the structure and morphology of MnO<sub>2</sub>-CuO/CF after an extensive 30-hour GOR was studied. As shown in Fig. 6a, MnO<sub>2</sub>-CuO/CF was able to maintain its catalytic activity after glycerol supplementation at 10-hour intervals. Following the GOR test, the size of catalyst remains unchanged, and the surface of the network structure becomes rough (refer to Fig. S16). The surface elemental analysis through EDS mapping revealed almost no reduction in the content of Mn and Cu. (refer to Fig. S14-S15). The structure stability of MnO<sub>2</sub>-CuO/CF electrodes were analyzed by XPS after electrochemical reaction (the wide scan survey spectra of MnO<sub>2</sub>-

CuO/CF after GOR is shown in Fig. S17). As depicted in Fig. 6b, XPS spectrum of Cu 2p on MnO<sub>2</sub>-CuO/CF, exhibited a peak at 931.7 eV, indicative of the presence of Cu<sup>0</sup>. This Cu<sup>0</sup> is attributed to the fact that MnO<sub>2</sub>-CuO/CF grows on copper foam. The XPS spectra of Mn 2p in MnO<sub>2</sub>-CuO/CF before and after the reaction revealed the presence of Mn<sup>4+</sup> and Mn<sup>3+</sup> states. After the electrochemical reaction, no discernible alterations were observed in the Cu 2p and Mn 2p spectra (Fig. 6b, c). The O 1s spectra show a peak corresponding to adsorbed oxygen at 532 eV, and its intensity increased after the long electrooxidation test (Fig. 6d). This phenomenon is also similar to other reports [25]. Further, *Operando* Raman spectroscopy (RXN1-532NM) was employed to gain a deeper understanding of the impact of voltage on MnO<sub>2</sub>-CuO/CF during GOR. The tests employed a 532 nm laser with 2-minute exposure duration, and the electrolyte composition consisted 1 M KOH and 0.1 M glycerol. Each voltage condition was assessed over a 1-hour period. The Fig. 6e showed that the Raman spectra of MnO<sub>2</sub> and CuO changed significantly at 500 (MnO<sub>2</sub>), 583 (MnO<sub>2</sub>) and 623 cm<sup>-1</sup> (CuO). At high voltages (1.5 V vs. RHE), these three peaks disappeared completely. This



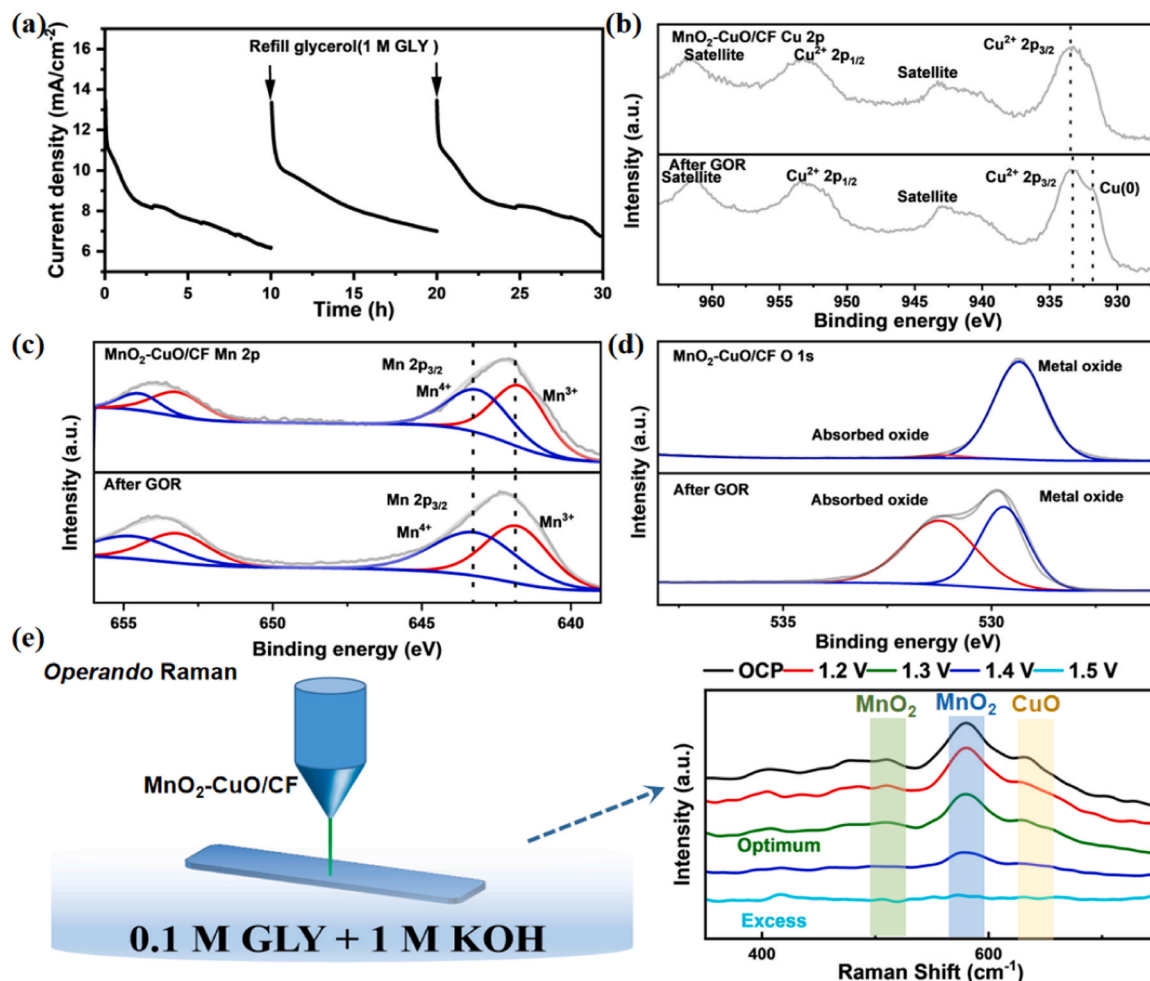


**Fig. 6.** (a) Electrolysis test at constant voltage (1.3 V vs. RHE) for 30 hours. (b-d) The XPS spectra of Cu 2p, Mn 2p, and O 1s before and after 30 h continuous GOR (MnO<sub>2</sub>-CuO/CF). (e) Operando Raman spectra at different applied potentials. Laser wavelength = 532 nm.

implies that MnO<sub>2</sub>-CuO/CF can keep a stable structure when operating at potentials below 1.4 V during GOR.

In order to evaluate the performance of MnO<sub>2</sub>-CuO/CF in more practical situations, we established a two-electrode electrolysis cell, using MnO<sub>2</sub>-CuO/CF as the anode and Pt/C catalyst as the cathode, combining the anode GOR and cathode HER together. Under long-term electrolysis for 100 hours, the catalytic current can still be maintained at 10 mA/cm<sup>2</sup> (Fig. S18), proving that MnO<sub>2</sub>-CuO/CF has high stability. The H<sub>2</sub> produced by the 10 hours reaction system was collected by the gas chromatography (Shanghai Ruimin GC-2060) and compared with the theoretical hydrogen production, as shown in Fig. S14a, indicating that stable H<sub>2</sub> production can be achieved with a Faraday efficiency of over 90%. The liquid phase products were collected by HPLC, and the main product DHA selectivity reached 60%, proving that the catalyst can achieve effective long-term coupling of GOR and HER. Under conditions of 1.3 V and 10 mA/cm<sup>2</sup>, the H<sub>2</sub> and DHA productivities were 0.31 and 0.38 mmol cm<sup>-2</sup> h<sup>-1</sup>.

### 3.3. DFT calculations

The oxidation of glycerol is a complex process that involves 14 electron transfer steps. Existing studies have shown that glycerol initially adsorbs on the catalyst surface to form intermediates, and this step significantly influences the oxidation process[52]. To gain insight into this adsorption pattern and to understand the reaction mechanism of glycerol oxidation to DHA, we conducted DFT calculations. Guided by HRTEM images and XRD patterns of MnO<sub>2</sub>-CuO/CF, where CuO (111)

and MnO<sub>2</sub> (100) facets were evident, CuO (111) facets and MnO<sub>2</sub> (100) as a basis were employed for DFT calculations. The adsorption energies (*E*<sub>ads</sub>) of glycerol terminal and intermediate hydroxyl groups on CuO (111) and MnO<sub>2</sub> (100) were mainly explored. As shown in Fig. 7a-d, a comparably close adsorption energy for the intermediate hydroxyl group on both crystalline surfaces was revealed. This indicates a synergies effect between the two surfaces in catalyzing the oxidation of glycerol. Furthermore, it is worth noting that the adsorption energy of the intermediate hydroxyl group (CuO Fig. 7a; MnO<sub>2</sub> Fig. 7c) on these surfaces is higher than that of the terminal hydroxyl group (CuO Fig. 7b; MnO<sub>2</sub> Fig. 7d). This discrepancy implies that easier oxidation of the intermediate hydroxyl group, leading to the formation of DHA is more favorable.

Moreover, compare to CuO (111), the adsorption energy of DHA (as illustrated in Fig. 7e, f) on MnO<sub>2</sub> (100) is much lower, which confirms that DHA is easier to desorb from MnO<sub>2</sub> (100). Fig. 7 h, i show the variance in electron density upon DHA adsorption on CuO (111) and MnO<sub>2</sub> (100) surfaces. These representations elucidate that MnO<sub>2</sub>-DHA induces a reduction in electron density.[53] MnO<sub>2</sub> is distributed on the surface of the catalytic electrode with a large specific surface area, and CuO grows in the inner layer of copper foam, the overlap configuration of CuO and MnO<sub>2</sub> is benefit for regulation of electron density on MnO<sub>2</sub>. Although CuO has a higher adsorption energy for DHA, it has a small contact area with the solution. MnO<sub>2</sub>, which is distributed on the outer side, has a lower electron density, and the adsorbed DHA is easier to desorb. This result can also be verified from the MnO<sub>2</sub>-CuO/CF XPS spectra (Fig. 3e, f), which has a higher Mn<sup>4+</sup> content compared to

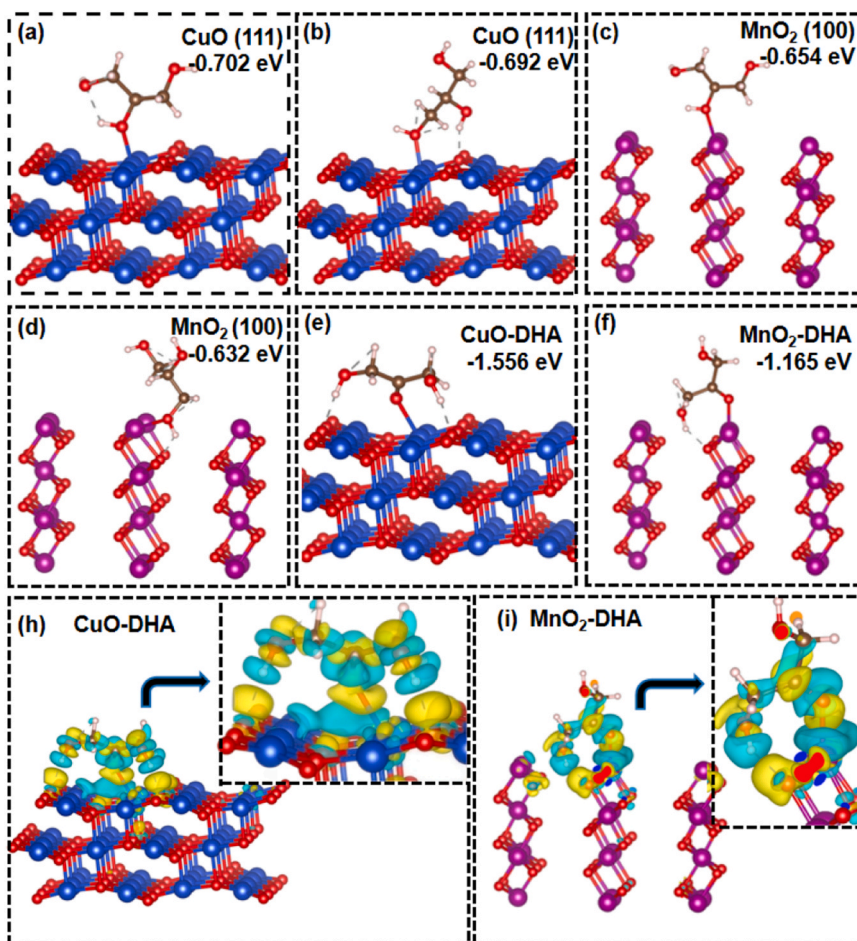


**Fig. 7.** (a, b) Adsorption energy of CuO (111) by glycerol sec-hydroxyl and terminal hydroxyl groups. (c, d) Adsorption energy of MnO<sub>2</sub> (100) by glycerol sec-hydroxyl and terminal hydroxyl group, (e, f) Adsorption energy of CuO (111) by DHA. (h, i) Electron density differences of CuO-DHA and MnO<sub>2</sub>-DHA (The yellow and cyan colors denote an increase and decrease of the charge density, respectively).

MnO<sub>2</sub>/CF. The expeditious desorption of DHA from MnO<sub>2</sub>-CuO/CF surface stands as a pivotal factor influencing its selectivity. The DFT calculation results further verified that MnO<sub>2</sub>-CuO/CF can improve the selectivity of DHA.

The glycerol oxidation to obtain DHA is seriously depending on voltage. According to the product analysis and pertinent literature[12, 25,54,55], we present a reaction pathway for glycerol electrooxidation with MnO<sub>2</sub>-CuO/CF (see Fig. 8). The theoretical oxidation potential of glycerol is 0.003 V vs. RHE. In an alkaline environment, glycerol's hydroxyl group undergoes oxidation to yield glyceraldehyde or DHA[56]. DFT calculations of adsorption energies indicates the preference for

generating DHA on MnO<sub>2</sub>-CuO/CF. As the voltage increases from 1.2 V to 1.4 V, the current density increases from 2.0 mA cm<sup>-2</sup> to 32.5 mA cm<sup>-2</sup>, indicating the activity increased with voltage. The concentration of DHA decreases from 60% to 35%, the concentration formic acid increases from 31% to 55%, confirming that oxidation potential is related to that of selectivity. Under strongly alkaline conditions, a fraction of DHA undergoes conversion to glyceraldehyde. Glyceraldehyde can further oxidize to glycerate and undergo subsequent C-C bond cleavage to yield oxalate or formate. These intermediates can be further oxidized to carbonates. Nevertheless, experimental observations reveal that when copper oxide solely acts as the catalyst, DHA tends to undergo

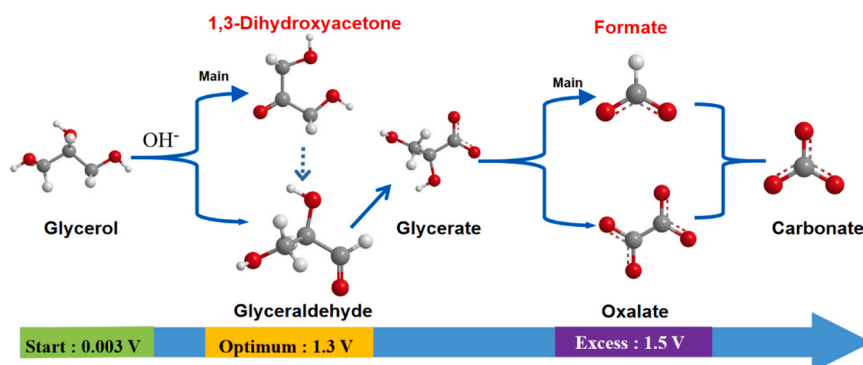


**Fig. 8.** Possible reaction pathway of MnO<sub>2</sub>-CuO/CF for GOR.

subsequent conversion to formic acid. To enhance DHA yield, rapid adsorption and desorption on the catalytic electrode to prevent over-oxidation of DHA are requested. According to DFT calculations, the main crystal surfaces ( $\text{MnO}_2$  (100) and  $\text{CuO}$  (111)) exhibit similar adsorption energies for glycerol. This may be attributed to the synergistic effect within  $\text{MnO}_2$  and  $\text{CuO}$ , favoring glycerol adsorption.  $\text{MnO}_2$  (100) exhibits a lower electron density with DHA (Fig. 7i) and  $\text{MnO}_2$  possesses greater specific surface area (Fig. 2e) exposing outside of  $\text{MnO}_2\text{-CuO/CF}$ , thus making it more conducive to the desorption of DHA. The XPS results (Fig. 3e, f) also proved that compared to  $\text{CuO/CF}$ , the AOS value of  $\text{MnO}_2\text{-CuO/CF}$  significantly increased. The comparative experiments and the XPS spectra showed that the selectivity of DHA obtained with  $\text{MnO}_2\text{-CuO/CF}$  was lower than that of  $\text{MnO}_2\text{-CuO/CF}$ , suggesting that  $\text{CuO}$  could effectively reduce the electron density of  $\text{MnO}_2$  and promote DHA desorption. Additionally, the band diagrams and relevant information of  $\text{CuO}$  and  $\text{MnO}_2$  is shown in Fig. S19.

#### 4. Conclusion

In summary, a composite  $\text{MnO}_2\text{-CuO/CF}$  electrode for GOR through an in-situ hydrothermal growth process on copper foam was developed. This catalyst attains a current density of  $10.7 \text{ mA cm}^{-2}$  at 1.3 V and demonstrates superior efficiency in producing DHA with a remarkable 60% average selectivity during 5 h test. *Operando* Raman assessments of the catalyst surface verified its performance, maintaining stability at voltages below 1.4 V. Through DFT calculations, XPS spectra and HPLC product analysis, we found that  $\text{MnO}_2\text{-CuO}$  has a synergistic effect during the oxidation process, which is able to adsorb glycerol to produce DHA. The overlap configuration of  $\text{CuO}$  and  $\text{MnO}_2$  is benefit for regulation of electron density on  $\text{MnO}_2$ .  $\text{MnO}_2$  is affected by  $\text{CuO}$  in the inner layer, resulting in lower electron density and higher AOS value. Additionally, its larger specific surface area is more conducive to the desorption of DHA, thereby improving its selectivity. By coupling GOR and water electrolysis to hydrogen, the dual output of high value-added organic products and high-purity hydrogen can be realized, which provides a new idea for green hydrogen production and electrochemical synthesis of high value-added chemicals.

#### CRediT authorship contribution statement

**Hongbin Zhao:** Supervision, Resources. **Daixin Ye:** Writing – review & editing. **Jiujun Zhang:** Supervision. **Ya Tang:** Formal analysis. **Hongji Ren:** Investigation. **Jian Guo:** Methodology. **Zijian Huang:** Writing – original draft.

#### Declaration of Competing Interest

The authors declare that they have no known competing financial interests or personal relationships that could have appeared to influence the work reported in this paper.

#### Data availability

The data that has been used is confidential.

#### Acknowledgements

We gratefully acknowledge financial support from the Key Research & Development Projects of Zhejiang Province (2019C01072), the National Natural Science Foundation of China (22002086, 22204096) and the Key Laboratory of Fuel Cell Technology of Guangdong Province.

#### Appendix A. Supporting information

Supplementary data associated with this article can be found in the online version at [doi:10.1016/j.apcatb.2024.123986](https://doi.org/10.1016/j.apcatb.2024.123986).

#### References

- [1] X. Yu, R.B. Araujo, Z. Qiu, E. Campos dos Santos, A. Anil, A. Cornell, L.G. M. Pettersson, M. Johansson, Hydrogen evolution linked to selective oxidation of glycerol over  $\text{CoMoO}_4$ —a theoretically predicted catalyst, *Adv. Energy Mater.* 12 (2022) 2103750, <https://doi.org/10.1002/aenm.202103750>.
- [2] W. Zhang, M. Liu, X. Gu, Y. Shi, Z. Deng, N. Cai, Water Electrolysis toward Elevated Temperature, *Adv., Chall. Front., Chem. Rev.* 123 (2023) 7119–7192, <https://doi.org/10.1021/acs.chemrev.2c00573>.
- [3] M. Guo, R. Deng, C. Wang, Q. Zhang, Recent progress of advanced manganese oxide-based materials for acidic oxygen evolution reaction: Fundamentals, performance optimization, and prospects, *J. Energy Chem.* 78 (2023) 537–553, <https://doi.org/10.1016/j.jechem.2022.11.054>.
- [4] Y. Zeng, M. Zhao, Z. Huang, W. Zhu, J. Zheng, Q. Jiang, Z. Wang, H. Liang, Surface Reconstruction of Water Splitting Electrocatalysts, *Adv. Energy Mater.* 12 (2022) 2201713, <https://doi.org/10.1002/aenm.202201713>.
- [5] H. Wu, Y. Wang, Z. Shi, X. Wang, J. Yang, M. Xiao, J. Ge, W. Xing, C. Liu, Recent developments of iridium-based catalysts for the oxygen evolution reaction in acidic water electrolysis, *J. Mater. Chem. A* 10 (2022) 13170–13189, <https://doi.org/10.1039/D1TA10324E>.
- [6] K. Veeramani, G. Janani, J. Kim, S. Surendran, J. Lim, S.C. Jesudass, S. Mahadik, H. Lee, T.-H. Kim, J.K. Kim, U. Sim, Hydrogen and value-added products yield from hybrid water electrolysis: A critical review on recent developments, *Renew. Sustain. Energy Rev.* 177 (2023) 113227, <https://doi.org/10.1016/j.rser.2023.113227>.
- [7] Z. Yu, C. Si, F. Sabaté, A.P. LaGrow, Z. Tai, V.M. Diaconescu, L. Simonelli, L. Meng, M.J. Sabater, B. Li, L. Liu, Defective Ru-doped  $\alpha\text{-MnO}_2$  nanorods enabling efficient hydrazine oxidation for energy-saving hydrogen production via proton exchange membranes at near-neutral pH, *Chem. Eng. J.* 470 (2023) 144050, <https://doi.org/10.1016/j.cej.2023.144050>.
- [8] Z. Li, Y. Yan, S.-M. Xu, H. Zhou, M. Xu, L. Ma, M. Shao, X. Kong, B. Wang, L. Zheng, H. Duan, Alcohols electrooxidation coupled with  $\text{H}_2$  production at high current densities promoted by a cooperative catalyst, *Nat. Commun.* 13 (2022) 147, <https://doi.org/10.1038/s41467-021-27806-3>.
- [9] Y. Li, X. Wei, L. Chen, J. Shi, M. He, Nickel-molybdenum nitride nanoplate electrocatalysts for concurrent electrolytic hydrogen and formate productions, *Nat. Commun.* 10 (2019) 5335, <https://doi.org/10.1038/s41467-019-13375-z>.
- [10] D.T. Tran, T.H. Nguyen, H. Jeong, P.K.L. Tran, D. Malhotra, K.U. Jeong, N.H. Kim, J.H. Lee, Recent engineering advances in nanocatalysts for  $\text{NH}_3$ -to- $\text{H}_2$  conversion technologies, *Nano Energy* 94 (2022) 106929, <https://doi.org/10.1016/j.nanoen.2022.106929>.
- [11] M. Zhang, H. Li, X. Duan, P. Zou, G. Jeerh, B. Sun, S. Chen, J. Humphreys, M. Walker, K. Xie, S. Tao, An efficient symmetric electrolyzer based on bifunctional perovskite catalyst for ammonia electrolysis, *advanced, Science* 8 (2021) 2101299, <https://doi.org/10.1002/adv.202101299>.
- [12] J. Wu, X. Yang, M. Gong, Recent advances in glycerol valorization via electrooxidation: Catalyst, mechanism and device, *Chin. J. Catal.* 43 (2022) 2966–2986, [https://doi.org/10.1016/S1872-2067\(22\)64121-4](https://doi.org/10.1016/S1872-2067(22)64121-4).
- [13] H. Luo, J. Barrio, N. Sunny, A. Li, L. Steier, N. Shah, I.E.L. Stephens, M.-M. Titirici, Progress and perspectives in photo- and electrochemical-oxidation of biomass for sustainable chemicals and hydrogen production, *Adv. Energy Mater.* 11 (2021) 2101180, <https://doi.org/10.1002/aenm.202101180>.
- [14] J. Shi, Q. Sun, J. Chen, W. Zhu, T. Cheng, M. Ma, Z. Fan, H. Yang, F. Liao, M. Shao, Z. Kang, Nitrogen contained rhodium nanosheet catalysts for efficient hydrazine oxidation reaction, *Appl. Catal. B: Environ.* 343 (2024) 123561, <https://doi.org/10.1016/j.apcatb.2023.123561>.
- [15] M.R. Monteiro, C.L. Kugelmeier, R.S. Pinheiro, M.O. Batalha, A. da Silva César, Glycerol from biodiesel production: Technological paths for sustainability, *Renew. Sustain. Energy Rev.* 88 (2018) 109–122, <https://doi.org/10.1016/j.rser.2018.02.019>.
- [16] M. Cerro-Alarcón, A. Corma, S. Iborra, C. Martínez, M.J. Sabater, Methanolysis of sunflower oil using gem-diamines as active organocatalysts for biodiesel production, *Appl. Catal. A: Gen.* 382 (2010) 36–42, <https://doi.org/10.1016/j.apcata.2010.04.024>.
- [17] J. Kaur, A.K. Sarma, M.K. Jha, P. Gera, Valorisation of crude glycerol to value-added products: Perspectives of process technology, *Econ. Environ. Issues, Biotechnol. Rep.* 27 (2020) e00487, <https://doi.org/10.1016/j.btre.2020.e00487>.
- [18] M. Braun, C.S. Santana, A.C. Garcia, C. Andronescu, From waste to value – Glycerol electrooxidation for energy conversion and chemical production, *Curr. Opin. Green. Sustain. Chem.* 41 (2023) 100829, <https://doi.org/10.1016/j.cogsc.2023.100829>.
- [19] Z. Liang, M.A. Villalba, G. Marcandalli, K. Ojha, A.J. Shih, M.T.M. Koper, Electrochemical reduction of the simplest monosaccharides: dihydroxyacetone and glyceraldehyde, *ACS Catal.* 10 (2020) 13895–13903, <https://doi.org/10.1021/acscatal.0c04131>.
- [20] M. Anitha, S.K. Kamarudin, N.T. Kofli, The potential of glycerol as a value-added commodity, *Chem. Eng. J.* 295 (2016) 119–130, <https://doi.org/10.1016/j.cej.2016.03.012>.
- [21] H. Mou, Q. Chang, Z. Xie, S. Hwang, S. Kattel, J.G. Chen, Enhancing glycerol electrooxidation from synergistic interactions of platinum and transition metal carbides, *Appl. Catal. B: Environ.* 316 (2022) 121648, <https://doi.org/10.1016/j.apcatb.2022.121648>.
- [22] A.C. Garcia, Y.Y. Birdja, G. Tremiliosi-Filho, M.T.M. Koper, Glycerol electro-oxidation on bismuth-modified platinum single crystals, *J. Catal.* 346 (2017) 117–124, <https://doi.org/10.1016/j.jcat.2016.12.013>.



- [23] A.C. Garcia, M.J. Kolb, C. Van Nierop y Sanchez, J. Vos, Y.Y. Birdja, Y. Kwon, G. Tremiliosi-Filho, M.T.M. Koper, Strong impact of platinum surface structure on primary and secondary alcohol oxidation during electro-oxidation of glycerol, *ACS Catal.* 6 (2016) 4491–4500, <https://doi.org/10.1021/acscatal.6b00709>.
- [24] T. Li, D.A. Harrington, An overview of glycerol electrooxidation mechanisms on Pt, Pd and Au, *ChemSusChem* 14 (2021) 1472–1495, <https://doi.org/10.1002/cssc.202002669>.
- [25] C. Liu, M. Hirohara, T. Maekawa, R. Chang, T. Hayashi, C.-Y. Chiang, Selective electro-oxidation of glycerol to dihydroxyacetone by a non-precious electrocatalyst – CuO, *Appl. Catal. B: Environ.* 265 (2020) 118543, <https://doi.org/10.1016/j.apcatb.2019.118543>.
- [26] Y. Li, X. Wei, S. Han, L. Chen, J. Shi, MnO<sub>2</sub> electrocatalysts coordinating alcohol oxidation for ultra-durable hydrogen and chemical productions in acidic solutions, *Angew. Chem. Int. Ed.* 60 (2021) 21464–21472, <https://doi.org/10.1002/anie.202107510>.
- [27] G.-S. Tran, T.-G. Vo, C.-Y. Chiang, Operando revealing the crystal phase transformation and electrocatalytic activity correlation of MnO<sub>2</sub> toward glycerol electrooxidation, *ACS Appl. Mater. Interfaces* 15 (2023) 22662–22671, <https://doi.org/10.1021/acsami.3c00857>.
- [28] S. Mourdikoudis, A. Kostopoulou, A.P. LaGrow, Magnetic nanoparticle composites: synergistic effects and applications, *Adv. Sci.* 8 (2021) 2004951, <https://doi.org/10.1002/adv.202004951>.
- [29] F. Sabaté, J. Navas, M.J. Sabater, A. Corma, Synthesis of  $\gamma$ -lactones from easily and accessible reactants catalyzed by Cu–MnOx catalysts, *Comptes Rendus Chim.* 21 (2018) 164–173, <https://doi.org/10.1016/j.crci.2017.10.001>.
- [30] Q. Liu, S. Wang, F. Han, S. Lv, Z. Yan, Y. Xi, J. Ouyang, Biomimetic tremelliform ultrathin MnO<sub>2</sub>/CuO nanosheets on kaolinite driving superior catalytic oxidation: an example of CO, *ACS Appl. Mater. Interfaces* 14 (2022) 44345–44357, <https://doi.org/10.1021/acsami.2c11640>.
- [31] Y. Yang, Y. Wang, X. Li, C. Xue, Z. Dang, L. Zhang, X. Yi, Effects of synthesis temperature on  $\epsilon$ -MnO<sub>2</sub> microstructures and performance: Selective adsorption of heavy metals and the mechanism onto (100) facet compared with (001), *Environ. Pollut.* 315 (2022) 120218, <https://doi.org/10.1016/j.envpol.2022.120218>.
- [32] G. Kresse, J. Hafner, Ab initio molecular-dynamics simulation of the liquid-metal-amorphous-semiconductor transition in germanium, *Phys. Rev. B* 49 (1994) 14251–14269, <https://doi.org/10.1103/PhysRevB.49.14251>.
- [33] G. Kresse, J. Furthmüller, Efficiency of ab-initio total energy calculations for metals and semiconductors using a plane-wave basis set, *Comput. Mater. Sci.* 6 (1996) 15–50, [https://doi.org/10.1016/0927-0256\(96\)00008-0](https://doi.org/10.1016/0927-0256(96)00008-0).
- [34] G. Kresse, D. Joubert, From ultrasoft pseudopotentials to the projector augmented-wave method, *Phys. Rev. B* 59 (1999) 1758–1775, <https://doi.org/10.1103/PhysRevB.59.1758>.
- [35] P.E. Blöchl, Projector augmented-wave method, *Phys. Rev. B* 50 (1994) 17953–17979, <https://doi.org/10.1103/PhysRevB.50.17953>.
- [36] K. Burke, J.P. Perdew, M. Ernzerhof, Why semilocal functionals work: Accuracy of the on-top pair density and importance of system averaging, *J. Chem. Phys.* 109 (1998) 3760–3771, <https://doi.org/10.1063/1.476976>.
- [37] M. Ernzerhof, G.E. Scuseria, Assessment of the Perdew–Burke–Ernzerhof exchange–correlation functional, *J. Chem. Phys.* 110 (1999) 5029–5036, <https://doi.org/10.1063/1.478401>.
- [38] K. Bholá, J.J. Varghese, L. Dapeng, Y. Liu, S.H. Mushrif, Influence of Hubbard U parameter in simulating adsorption and reactivity on CuO: combined theoretical and experimental study, *J. Phys. Chem. C* 121 (2017) 21343–21353, <https://doi.org/10.1021/acs.jpcc.7b05385>.
- [39] Y. Maimaiti, M. Nolan, S.D. Elliott, Reduction mechanisms of the CuO(111) surface through surface oxygen vacancy formation and hydrogen adsorption, *Phys. Chem. Chem. Phys.* 16 (2014) 3036–3046, <https://doi.org/10.1039/C3CP53991A>.
- [40] Y. Jiang, L. Yuan, X. Wang, W. Zhang, J. Liu, X. Wu, K. Huang, Y. Li, Z. Liu, S. Feng, Jahn–Teller disproportionation induced exfoliation of unit-cell scale  $\epsilon$ -MnO<sub>2</sub>, *Angew. Chem. Int. Ed.* 59 (2020) 22659–22666, <https://doi.org/10.1002/anie.202010246>.
- [41] Z. Cao, W. Zhang, R. Ding, J. Wang, M. Pu, Z. Yang, M. Lei, The reaction paths of CH<sub>2</sub>O decomposition on CuO(111) surface: a DFT study, *J. Phys. Org. Chem.* 33 (2020) e4017, <https://doi.org/10.1002/poc.4017>.
- [42] L. Bigiani, T. Andreu, C. Maccato, E. Fois, A. Gasparotto, C. Sada, G. Tabacchi, D. Krishnan, J. Verbeeck, J.R. Morante, D. Barreca, Engineering Au/MnO<sub>2</sub> hierarchical nanoarchitectures for ethanol electrochemical valorization, *J. Mater. Chem. A* 8 (2020) 16902–16907, <https://doi.org/10.1039/D0TA05972B>.
- [43] X. Deng, C. Wang, M. Shao, X. Xu, J. Huang, Low-temperature solution synthesis of CuO/Cu<sub>2</sub>O nanostructures for enhanced photocatalytic activity with added H<sub>2</sub>O<sub>2</sub>: synergistic effect and mechanism insight, *RSC Adv.* 7 (2017) 4329–4338, <https://doi.org/10.1039/C6RA27634B>.
- [44] Q. Simon, D. Barreca, A. Gasparotto, C. Maccato, T. Montini, V. Gombac, P. Fornasiero, O.I. Lebedev, S. Turner, G. Van Tendeloo, Vertically oriented CuO/ZnO nanorod arrays: from plasma-assisted synthesis to photocatalytic H<sub>2</sub> production, *J. Mater. Chem.* 22 (2012) 11739–11747, <https://doi.org/10.1039/C2JM31589K>.
- [45] Y. Yang, J. Huang, S. Wang, S. Deng, B. Wang, G. Yu, Catalytic removal of gaseous unintentional POPs on manganese oxide octahedral molecular sieves, *Appl. Catal. B: Environ.* 142–143 (2013) 568–578, <https://doi.org/10.1016/j.apcatb.2013.05.048>.
- [46] H. Yu, W. Wang, Q. Mao, K. Deng, Z. Wang, Y. Xu, X. Li, H. Wang, L. Wang, Pt single atom captured by oxygen vacancy-rich NiCo layered double hydroxides for coupling hydrogen evolution with selective oxidation of glycerol to formate, *Appl. Catal. B: Environ.* 330 (2023) 122617, <https://doi.org/10.1016/j.apcatb.2023.122617>.
- [47] S. Lee, H.J. Kim, E.J. Lim, Y. Kim, Y. Noh, G.W. Huber, W.B. Kim, Highly selective transformation of glycerol to dihydroxyacetone without using oxidants by a PtSb/C-catalyzed electrooxidation process, *Green Chem.* 18 (2016) 2877–2887, <https://doi.org/10.1039/C5GC02865E>.
- [48] Y. Kim, H.W. Kim, S. Lee, J. Han, D. Lee, J.-R. Kim, T.-W. Kim, C.-U. Kim, S.-Y. Jeong, H.-J. Chae, B.-S. Kim, H. Chang, W.B. Kim, S.M. Choi, H.-J. Kim, The role of ruthenium on carbon-supported PtRu catalysts for electrocatalytic glycerol oxidation under acidic conditions, *ChemCatChem* 9 (2017) 1683–1690, <https://doi.org/10.1002/cctc.201601325>.
- [49] T.-G. Vo, P.-Y. Tsai, C.-Y. Chiang, Tuning selectivity and activity of the electrochemical glycerol oxidation reaction by manipulating morphology and exposed facet of spinel cobalt oxides, *J. Catal.* 424 (2023) 64–73, <https://doi.org/10.1016/j.jcat.2023.05.010>.
- [50] G.-S. Tran, T.-G. Vo, C.-Y. Chiang, Earth-abundant manganese oxide nanoneedle as highly efficient electrocatalyst for selective glycerol electro-oxidation to dihydroxyacetone, *J. Catal.* 404 (2021) 139–148, <https://doi.org/10.1016/j.jcat.2021.09.005>.
- [51] J. Wu, J. Li, Y. Li, X.-Y. Ma, W.-Y. Zhang, Y. Hao, W.-B. Cai, Z.-P. Liu, M. Gong, Steering the glycerol electro-reforming selectivity via cation–intermediate interactions, *Angew. Chem. Int. Ed.* 61 (2022) e202113362, <https://doi.org/10.1002/anie.202113362>.
- [52] M. Simões, S. Baranton, C. Coutanceau, Electrochemical valorisation of glycerol, *ChemSusChem* 5 (2012) 2106–2124, <https://doi.org/10.1002/cssc.201200335>.
- [53] Z. Shen, Z. Zhang, M. Li, Y. Yuan, Y. Zhao, S. Zhang, C. Zhong, J. Zhu, J. Lu, H. Zhang, Rational design of a Ni<sub>3</sub>N<sub>0.85</sub> electrocatalyst to accelerate polysulfide conversion in lithium–sulfur batteries, *ACS Nano* 14 (2020) 6673–6682, <https://doi.org/10.1021/acsnano.9b09371>.
- [54] X. Hu, J. Lu, Y. Liu, L. Chen, X. Zhang, H. Wang, Sustainable catalytic oxidation of glycerol: a review, *Environ. Chem. Lett.* 21 (2023) 2825–2861, <https://doi.org/10.1007/s10311-023-01608-z>.
- [55] Y. Kwon, Y. Birdja, I. Spanos, P. Rodriguez, M.T.M. Koper, Highly Selective Electro-Oxidation of Glycerol to Dihydroxyacetone on Platinum in the Presence of Bismuth, *ACS Catal.* 2 (2012) 759–764, <https://doi.org/10.1021/cs200599g>.
- [56] A. Garcia, M. Kolb, C. van Nierop, Y. Sanchez, J. Vos, Y. Birdja, Y. Kwon, G. Tremiliosi-Filho, M. Koper, Strong impact of platinum surface structure on primary and secondary alcohol oxidation during electro-oxidation of glycerol, *ACS Catal.* 6 (2016), <https://doi.org/10.1021/acscatal.6b00709>.